Assembly of protein stacks with in-situ synthesised nanoparticle cargo

Sesha Manuguri[1,2,5], Kyle Webster[3] , Amy Yewdall[3,4], Yiran An[1], Hari Venugopal[3], Vaibhav Bhugra[2], Adrian Turner[3], Laura Domigan[2,3], Juliet A. Gerrard[1,2,3], David E. Williams[1,2] and Jenny Malmström[2,4*]

[1]*School of Chemical Sciences, University of Auckland, 92019, Auckland, New Zealand*
[2]*MacDiarmid Institute for Advanced Materials and Nanotechnology, Wellington, New Zealand*
[3]*School of Biological Sciences, University of Auckland, 92019, Auckland, New Zealand*
[4]*Biomolecular Interaction Centre and School of Biological Sciences, University of Canterbury, Christchurch 8140, New Zealand*
[5]*Department of Chemical and Materials Engineering, University of Auckland, 92019, New Zealand.*

Abstract

The ability of proteins to form hierarchical structures through self-assembly provides an opportunity to synthesize and organize nanoparticles. Ordered nanoparticle assemblies are a subject of wide interest due to the potential to harness their emergent functions. In this work, the toroidal shaped form of the protein peroxiredoxin which has a pore size of 7 nm was used to organize iron oxyhydroxide nanoparticles. Iron in the form of Fe^{2+} was sequestered into the central cavity of the toroid ring using metal binding sites engineered there, then hydrolysed to form oxyhydroxide particles bound into the protein pore. By precise manipulation of the pH, the mineralized toroids were organized into stacks confining one dimensional nanoparticle assemblies. We report the formation and the procedures leading to the formation of such nanostructures, and their characterization by chromatography and microscopy. Electrostatic force microscopy clearly revealed the formation of iron hydroxide nanorods, as a result of the self-assembly of the iron-loaded protein. This research augurs well for the use of peroxiredoxin as a template to form nanowires and structures for electronic and magnetic applications.

Key words: Protein nanotechnology, Peroxiredoxin, Iron oxide-mineralization, Nanoparticle organization, Electrostatic force microscopy (EFM)

Biomolecule templated synthesis and organization of inorganic nanoparticles is a bottom-up approach with potential to achieve size regimes that are not accessible through conventional synthetic routes. Linear biomolecules such as DNA and RNA have been used to synthesize and organize nanoparticles: [1-5] however, the lack of chemical and structural diversity is a limitation of these systems. Proteins, on the other hand, have evolved to function in the form of organized assemblies. These

assemblies exist in diverse forms, such as cages[6, 7], rods[8], toroids[9] and barrels[10]. Proteins have a large array of functional groups available through the amino-acids side chains, and additional functional groups can be inserted by genetic engineering as natural or unnatural amino acids [11] This has led to the development of a number of proteins as building blocks for nanotechnology.[12-17]

Iron mineralization is particularly interesting due to the potential for forming magnetic nanoparticles, which in turn can be organized through solution or surface self-assembly of the biological molecules.[18-21]Useful proteins for iron mineralization include the iron storage cage protein ferritin[22, 23] as well as other cage proteins such as cowpea chlorotic mottle virus (CCMV)[24] and cowpea mosaic virus (CPMV)[25]. A common strategy for nanoparticle mineralization is to modify the interior of the cage protein with amino acid residues that alter the surface electrostatics. This allows for binding of the desired metal ions or formation of the desired mineral phase.[7, 26-28] Thus far, such mineralization studies for nanoparticle synthesis have been mainly restricted to cage proteins.

In this work, we grow nanoparticles, *in-situ,* in protein rings, and organize them into one dimensional nanoparticle assemblies by exploiting the inherent stacking ability of the toroidal protein peroxiredoxin (Prx).Prx forms a range of macromolecular assemblies such as toroids, stacks, tubes, catenanes and cages, [29-31] in response to certain environmental stimuli, which offers the possibility to control the formation of such structures. Typically, in oxidative conditions Prx exists as homodimers, with disulphide bonds between the monomers. However, in reducing conditions, Prx form dodecameric toroidal shaped assemblies with an inner pore size of 7-8 nm.[32]Histidine-tagged constructs of Prx were shown to stabilise the toroidal form in both reducing and oxidising conditions.[33] These toroids stack into higher order structures in response to certain environmental stimuli, such as change in pH or salt concentration.[32, 34, 35]

While protein cages are generally not well-suited for the creation of continuous structures, some successful examples include the organization of negatively charged virus cages using positively charged polymers,[36, 37] and tuneable magnetic assemblies of ferritin created using the same electrostatic strategy.[38] Metal ion or nanoparticle induced self-assembly of proteins is another strategy to build hybrid organic-inorganic assemblies.[39, 40] GroEL, a barrel shaped multimeric protein has also been extensively exploited for its structural properties. For example, cysteine residues have been engineered to occur at the protein surface to append spiropyran moieties used as metal coordination sites to generate anisotropic cylindrical architectures of GroEL.[41, 42] Ring- or toroidal shaped proteins are particularly suited as building blocks for continuous hybrid structures. Stable protein 1,[43-46] heat shock protein TF55β[47] and heme carrier protein[48] have all been used as templates to synthesize, bind and assemble nanoparticles with emergent functions. Tobacco mosaic virus (TMV) is one of the plant viruses that have been particularly useful for the creation of anisotropic structures.[49] TMV is a hollow protein tube formed by helically arranged protein subunits and this has been used to template anisotropic hybrid metal nanostructures, such as metal oxides,[50] nickel-tin alloys,[51] metal nanowires[52, 53] and noble metal nanoparticles[53-55] Peroxiredoxins have also previously been used to produce hybrid assemblies, such

as binding of gold and palladium nanoparticles and to drive the stacking of graphene oxide layers.[56, 57] However, the present study is the first to construct extended hybrid assemblies using the pH triggered stacking of bio- mineralised peroxiredoxin.

Here, we use a stabilized toroidal form of peroxiredoxin with a pore lined with 72 histidine residues. Inspired by the way microbes mineralize iron oxides[58, 59] and the ability of ferritins to sequester iron,[22] we designed a ligand controlled approach to selectively nucleate iron oxyhydroxide nanoparticles inside the histidine functionalized pore of toroid Prx. We then used the ability of Prx to stack to organize these nucleated iron oxide nanoparticles into one-dimensional assemblies (Figure 1).

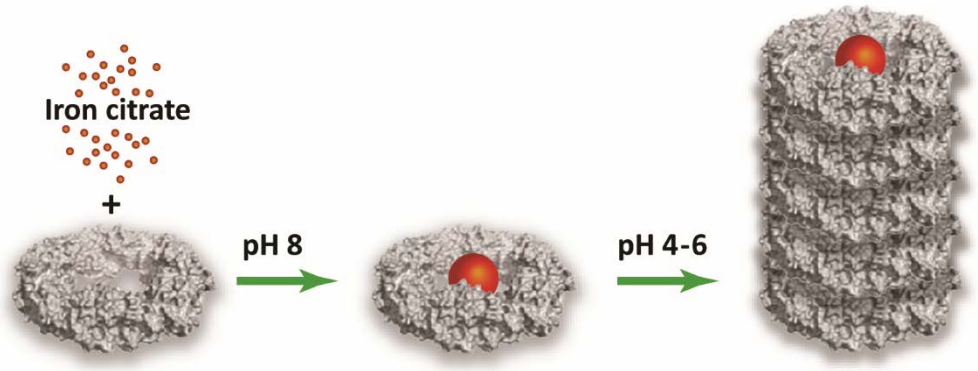

Figure 1 Schematic illustration depicting the process of 1-D nanoparticle assembly formation

To create small iron-containing particles inside the protein pore, we exploit the 6-histidine tag, which decorates the central pore and binds divalent metal ions [60] Iron, as Fe^{2+}, was sequestered into the pore. We predicted that the pore-sequestered Fe^{2+} would undergo oxidation in the presence of oxygen, leading to the formation of an iron oxyhydroxide particle within the protein pore. However, the presence of oxygen also leads to the oxidation of Fe^{2+} to Fe^{3+} in solution and in an initial attempt it was found that the poor solubility of Fe^{3+} at pH>6 (Prx is a stable single ring at pH 8.0[61]) led to large scale oxidative precipitation of iron oxyhydroxides along with the protein. To address this issue, we introduced citrate as a competitive ligand to the protein containing buffer. This promoted the precipitation of the iron oxyhydroxide inside the protein ring whilst avoiding precipitation in the solution. Although citrate is known to catalyse the oxidation of Fe(II) to Fe(III),[62] the solution is stabilised by the strong complexation of Fe(III) with citrate.[63] The stability constants of the Fe(II) complexes with histidine (Log K= 5.89) and citrate (Log K= 4.40), allows Fe(II) to partition between the solution and the protein core.[64] Additionally, we cooled the solution to 4°C to slow the oxidation.

The resulting protein sample was purified and characterised using size exclusion chromatography (SEC), inductively coupled plasma mass spectrometry (ICP-MS) and transmission electron microscopy (TEM) (Figure 2).SEC separates proteins depending on their size, with larger proteins eluting earlier than smaller proteins. From the absorption spectra of Fe-Prx and Prx (Figure S1), two detectors were

chosen, to detect the protein (absorbing at 280 nm) and the iron oxide (broad absorption, detected at 350 nm) simultaneously The SEC clearly shows that the Prx remains as a ring even after the iron binding, with a few larger assemblies apparent (ring eluting at 14.5 ml ~250 kDa). In all cases, the iron is detected to co-elute with the protein (no 350 nm signal is detected for the Prx control (Figure 2A)), indicating a successful sequestration of iron into the protein ring. The complete SEC profile of Fe-Prx (Figure S2) show that the unbound citrate complexes of Fe^{2+} elute at the retention volume of 20 mL (Figure S3). ICP-MS confirmed the presence of iron co-eluting with the protein. The inset in Figure 2B show the estimated iron content for each aliquot analysed. These data were pooled across the whole SEC peak and used, in combination with the estimated protein concentration, to arrive at an approximated loading of 220 iron atoms per Prx ring.

The retention of the protein ring was also confirmed by TEM as seen in Figure 2E (compared to the Prx control in Figure 2D). While in many cases, the protein ring exhibits a dark centre which could be indicative of a central iron containing particle, these images were taken using standard negative stain procedures which make conclusions of particle loading from these images challenging. From manual inspection of the TEM images, the protein ring was measured to be 15±1.5 nm in diameter with a 7 nm core, in correspondence with previously published data by Yewdall et al.[34] which confirmed a dodecameric ring.

To verify our hypothesis that the central histidine tags are driving the mineralisation in our case, we performed a control experiment using a wild type Prx without the histidine tag. In this case, the iron is not seen to elute with the protein ring in the SEC profile (Figure 2C). This demonstrates the importance of the histidine tag to sequester iron from the solution. This is in contrast to (for example) cage proteins such as *Listeria innocua Dps*, where it has been shown that mineralization can proceed without the aid of catalytic amino acid residues in the core of the protein.[65] The SEC in Figure 2C (full spectra available in Figure S4) confirms that the wild type Prx remains as a ring, but due to the less stable nature of the wild type protein compared to the mutant used in this paper, there is visible dissociation to dimers in the TEM image (Figure 2F) taken a day later and also on the SEC. To corroborate the dimer dissociation, a SEC profile of a mutant which doesn't form a ring and stays as dimer is shown in Figure S5.

In order to visualise the iron mineralisation in the protein without potential artefacts from the stain, we acquired unstained TEM images (Figure S6). The size of the mineralised iron oxide core was measured to be 4±1 nm (Figure S6B)

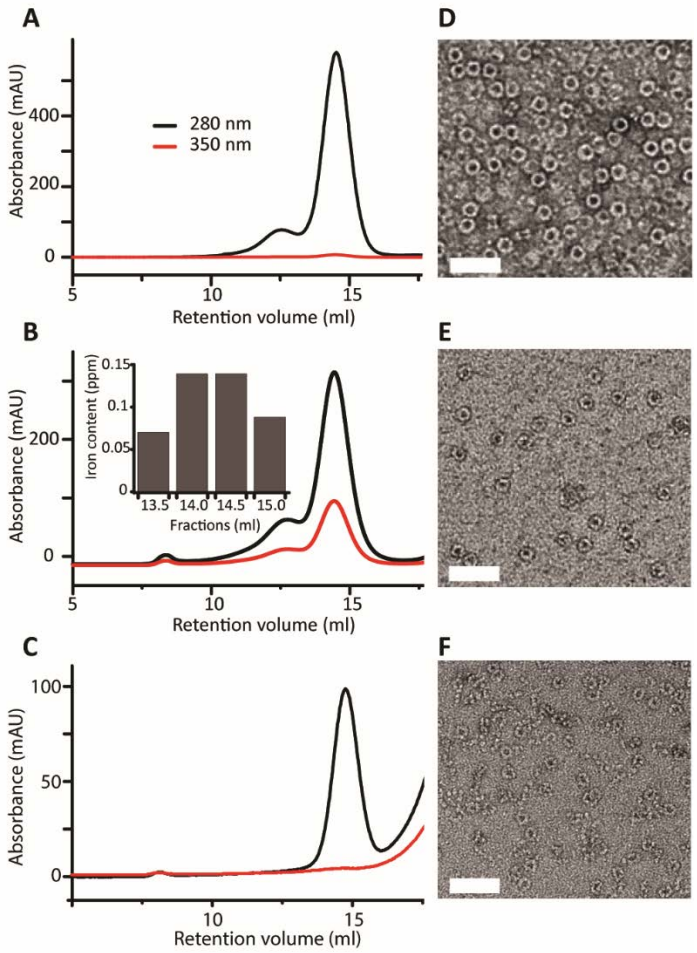

Figure 2: Size exclusion chromatography of A) Prx control B) Fe-Prx (Inset: Estimated iron content from ICP-MS for the four aliquots collected under the protein peak) and C) wild-type Prx without histidine tag exposed to mineralisation conditions. D) Negative stained TEM image of Prx E) Fe-Prx and F) wild-type Prx devoid of histidine-tag. The scale bar in the TEM images correspond to 50 nm.

The proteins were also imaged using tapping mode Atomic Force Microscopy (AFM) in both air and liquid environments. For these images, a dilute protein solution of either Fe-Prx or Prx was deposited onto freshly cleaved mica from a buffer solution containing divalent cations to facilitate surface interaction. Figure 3 shows images of Fe-Prx and Prx under liquid or ambient conditions. The images reveal intact protein rings with a clearly resolved central cavity in both the mineralized and un-mineralized protein. Due to the tip broadening effect of AFM,[66] the lateral dimension was not measured from the AFM images. Instead the height of the surface features was quantified. The topographic images in Figure 3 revealed an average height in liquid of 4.1±0.4 and 3.8±0.3 nm for Fe-Prx and Prx respectively. This height closely matches the x-ray crystal structure, from which the thickness of the protein toroid was found to be 4 nm.[32] Qualitatively, Fe-Prx appeared more firmly attached to the surface than its un-mineralised counterpart (easier to image in both liquid and air, data not shown). Fe-Prx also appeared more strictly round in shape under AFM. This observation may be due to an effect

of a stronger surface adsorption of Fe-Prx, making it less likely to move between scanlines, or it may be a true observation of the protein shape. When imaged in air, a considerably smaller height was measured for Prx (0.43±0.05 nm) (Figure 3D), as expected due to dehydration and compaction of the protein in the dried state. Similar results have been reported in the literature for CPMV and SP1 proteins and referred to as effects due to surface-protein interactions.[43, 67] Fe-Prx however, did not show this reduction in height when imaged in air; in fact it did not diminish in height at all. This result is in line with a mechanical reinforcement of the protein ring by the iron mineralization, as already qualitatively suggested by the liquid imaging. While it is possible that changes in imaging conditions could contribute to such effects, the images were acquired taking particular care to use consistent imaging conditions, using the same cantilever and identical imaging conditions such as amplitude set point/free air amplitude and scan rate.

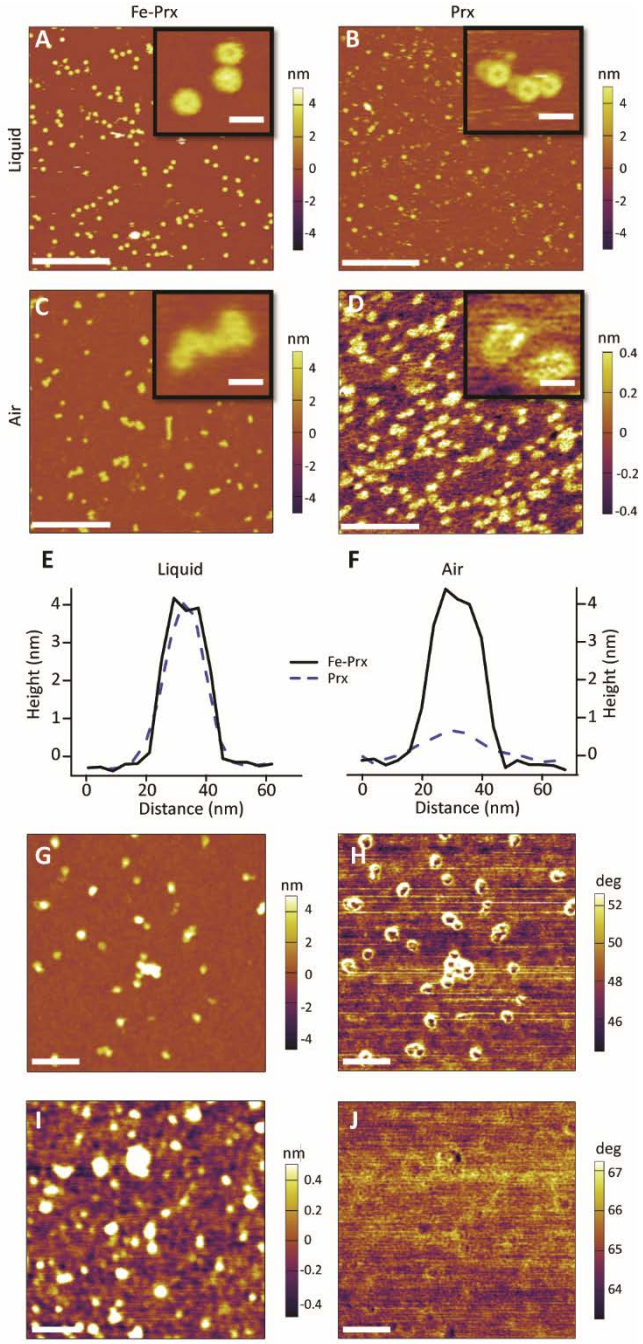

Figure 3: Tapping mode AFM images of protein deposited on freshly cleaved mica. Fe-Prx in liquid (A) and air (C) and the Prx control in liquid (B) and air (D) with scale bars in the image corresponding to 200 nm and 25 nm in the insets. Examples of topographical profiles of single Fe-Prx (solid line) and Prx (dotted line) imaged in liquid and air are shown in E and F respectively. Topography and phase contrast imaging in repulsive mode, performed in air on Fe-Prx (G,H) and Prx control (I,J) deposited on silicon wafers. Scale bars in G-J is 100 nm.

To further verify the presence of a nanoparticle inside the protein toroid, a phase contrast image of Fe-Prx was obtained in air. Phase contrast images, when acquired in repulsive mode, in AFM can reveal differences in material properties (hard or soft).[68] In the image of Prx, there was no observable phase contrast. However, for Fe-Prx the outer protein shell exhibited a brighter phase image

compared to the pore, again suggesting successful formation of iron oxide mineral core in the protein core. (Figure 3G-J))

With the aim to use Fe-Prx as a building block to create one dimensional nanoparticle assemblies, we investigated whether Fe-Prx retained the ability to form protein stacks upon reducing the pH as previously demonstrated for Prx.[32-35] To study this, the purified fraction of Fe-Prx or the Prx control was dialysed into citrate buffer at pH 4.0, 6.0 and 6.8 overnight at 4°C to allow for the formation of higher order structures. The stacking at intermediate pH (around pH 7.2) previously demonstrated for the his-tagged Prx[33] is mediated by the interactions between the charged histidine residues (pI 7.5[69]), while the stacking at lower pH (pH 4.0), is driven by the salt bridges formed between glutamic acid, lysine and histidine residues on the interfaces between the rings.[34] In our case, we have a his-tagged protein, but we have used this tag to sequester the iron and thus it was unclear at which pH the mineralized protein would stack. As evident from the TEM images in Figure 4 (pH 6.0) and Figure S7 (pH 4.0), dialysis to lower pH led to stacking of both Fe-Prx and the Prx control (Figure S8). Interestingly, an intermediate pH of 6.8 revealed short stacks only of the Prx, but not the Fe-Prx (Figure S9), attributed to the engagement of the histidine tags in iron binding.

The negatively stained TEM images for Fe-Prx clearly reveal one-dimensional stacked structures of individual mineralized rings similar to the Prx control.
Unstained grids were used to image the particles eliminating potential artefacts from the stain. Such unstained images revealed small nanoparticles, confirmed by EDX to be iron containing (Figure S10).

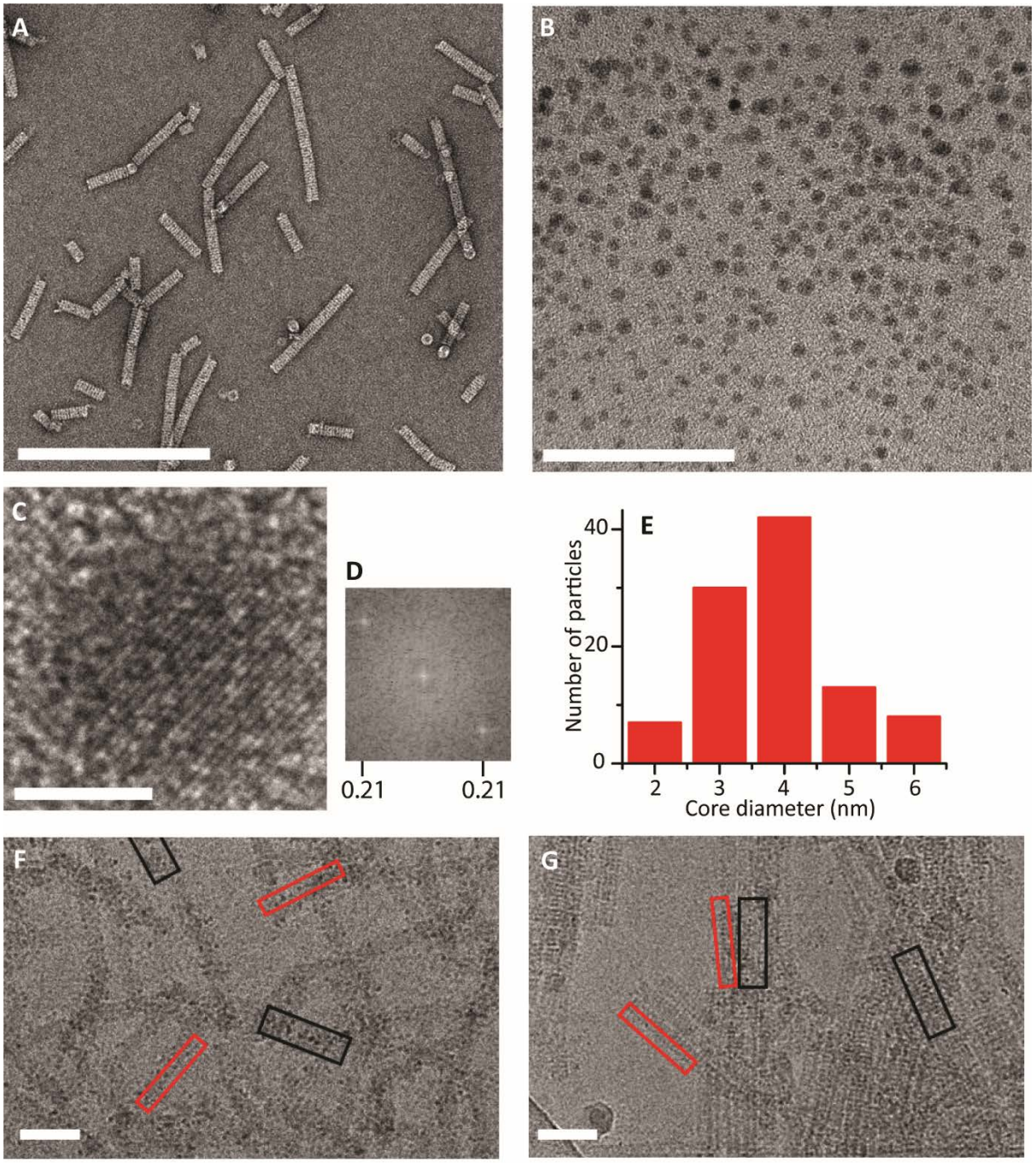

Figure 4: TEM imaging of Fe-Prx dialysed to pH 6.0. A) Negatively stained Fe-Prx assemblies (scale bar 100 nm) B) Corresponding unstained image (scale bar 50 nm) C) HR-TEM image obtained from the unstained sample (scale bar 3 nm) and its corresponding Fast Fourier Filtered (FFT) transform (D), with distances labelled in nm. E) Particle size distribution of iron oxyhydroxide particles, determined from unstained images analysed manually using image J, 100 particles were manually picked (in a random manner), and binned into 1 nm intervals for this graphic. F-G) Cryo-TEM of Fe-Prx dialysed to pH 6.0 (F) or pH 4.0 (G). Examples of particle association to the core of the protein tubes have been indicated with black boxes and examples of particle association with the outside of the tubes have been indicates with red boxes. The scale bars in F-G correspond to 50 nm.

During the imaging of the unstained grids, it was evident that the particles were unstable under the electron beam. The image presented in Figure 4B was acquired in low-dose mode and correspond to their original state. When imaging was allowed to proceed in the same area, the particles were seen to coalesce and enlarge over time (Figure S11). It is well known that unstained proteins are unstable under the electron beam, in particular using high voltages. Therefore, we interpret this coalescing of particles as being due to the protein shell being removed by the beam-damage. The early images however, show monodisperse nanoparticles whose average size was found to be 4.6±0.9 nm (Figure 4B & E). High resolution TEM (HR-TEM) and its corresponding FFT (Figure 4D) revealed that the particles have a d-spacing value of 0.21 nm corresponding to the crystalline ferrihydrite phase[70, 71] regardless of pH or stacking state (Figure S7D).Complementary analysis of a bulk precipitate obtained from a protein free solution ($FeSO_4$ added to buffer containing amino acid histidine) was performed using powder X-ray diffraction (XRD) and identified as lepidocrocite/goethite (95/5 mass ratio) (Figure S12). Such a difference in the crystal structure was previously found in the case of iron oxide mineralization in the presence of heat shock protein cage from *Methanococus janachii*[72] and interpreted as poorly crystalline ferrihydrite due to the absence of large d-spacing reflections in the mineralized protein.

To further investigate the position of the particles within the protein stacks, cryo-TEM images of Fe-Prx were acquired at pH 6.0 and 4.0 (Figure 4 F-G)). Cryo-TEM images revealed an interesting aspect of nanoparticle-Prx organization. Large stacks of Fe-Prx with nanoparticles were seen; however, it is clear that the particles are released from the histidine-lined protein pore as the pH is being lowered and the histidines become deprotonated. At pH 6.0, some particles are seen to be associated within the core of the protein tubes (exemplified with black boxes in Figure 4F and Figure S13B). However, the majority of the particles appear to be associated to the outer surface of the protein tube, along the length of the stack (indicated byred boxes in Figure 4G and Figure S13A). At pH 4.0, a relatively large proportion of the particles are seen to have been lost from the protein assemblies.

Electrostatic force microscopy (EFM) has emerged as a powerful technique to image materials based on electrostatic polarizability, surface potential or charge localisation in conducting materials.[73] Here, we explored the formation of higher order assemblies of mineralized Fe-Prx using EFM. A typical EFM experiment is done in a two pass mode. In the first pass, the topography of the sample is recorded. In the second pass, a potential difference is applied between the conducting tip and the substrate, and the tip is lifted to a height above the Van der Waals interaction height (~10 nm), following the topography, and recording the phase shift.[74, 75]

A solution containing Fe-Prx was adjusted to pH 6.0 (Figure 5) or pH 4.0 (Figure S11) respectively, and was deposited onto a p-doped silicon wafer in order to probe electrostatic forces at both positive and negative bias voltages of +5 V and -5 V. For Fe-Prx, the topography image showed protein stacks, and an EFM phase

response at both positive and negative potential biases, along the length of the protein stack. This EFM phase demonstrates the presence of a polarizable object, associated with the protein stack. The lack of EFM phase contrast in the control Prx sample (Figure 5J-K) confirms that the origin of the signal is from the nanoparticle association with the protein, in this case an iron oxyhydroxide nanoparticle, and not the protein itself, or any other ions associated with the histidine-tags The higher phase difference between Prx control and Fe-Prx stacks indicates the insulating and conductive nature of the materials. Similar phase behavior was seen previously in case of conducting and insulating PEO fibers.[76]No EFM phase response was observed at 0 V for Fe-Prx. Similar EFM phase responses were observed for one dimensional nanoparticle assemblies formed at pH 4 (Figure S14), indicating the retention of enough nanoparticles at this substantially lower pH to evoke an EFM phase signal. In addition, negative phase profiles were obtained regardless of the sign of the bias (Figure 5F and G) Average phase shifts of 20 Fe-Prx stacks obatined at 5 different locations of the sample were used to quantify the negative phase shift trend of Fe-Prx assemblies (Figure 5L). In addition, to further validate the results, the effect of lift heights (30-100 nm) on the EFM phase response, was observed at a fixed voltage of 6 V (Figure S15) . With increasing lift height, the average phase shift obtained on the fiber decreased as expected. This result confirms that the effect of height difference on the electrostatic interactions between the tip and stacks of Fe-Prx was negligible even when the Z feed back was off during the scan. Similarly to probe the effect of voltage, EFM phase response of Fe-Prx stacks was measured at voltages from 0 to 6 V (Figure S16). At 0 and 1 V, no EFM phase response was obtained. However, with increasing voltage a clear EFM phase response can be seen with average phase shift decreasing from -0.38º to -3.72º confirming the negative phase shift response. This result indicates that the nature of the electrostatic interaction between the Fe-Prx stack and tip is attractive, due to the polarizability of the Prx-nanoparticle assembly.[74, 77, 78] EFM studies were also carried out on Fe-Prx rings at a lift height of 15 nm and they elicited an EFM phase response as well (Figure S17). The combination of topographic and electrostatic information obtained from AFM and EFM studies confirmed the assembly of the iron hydroxide nanoparticles by Prx and the organization into one-dimensional macromolecular assemblies.

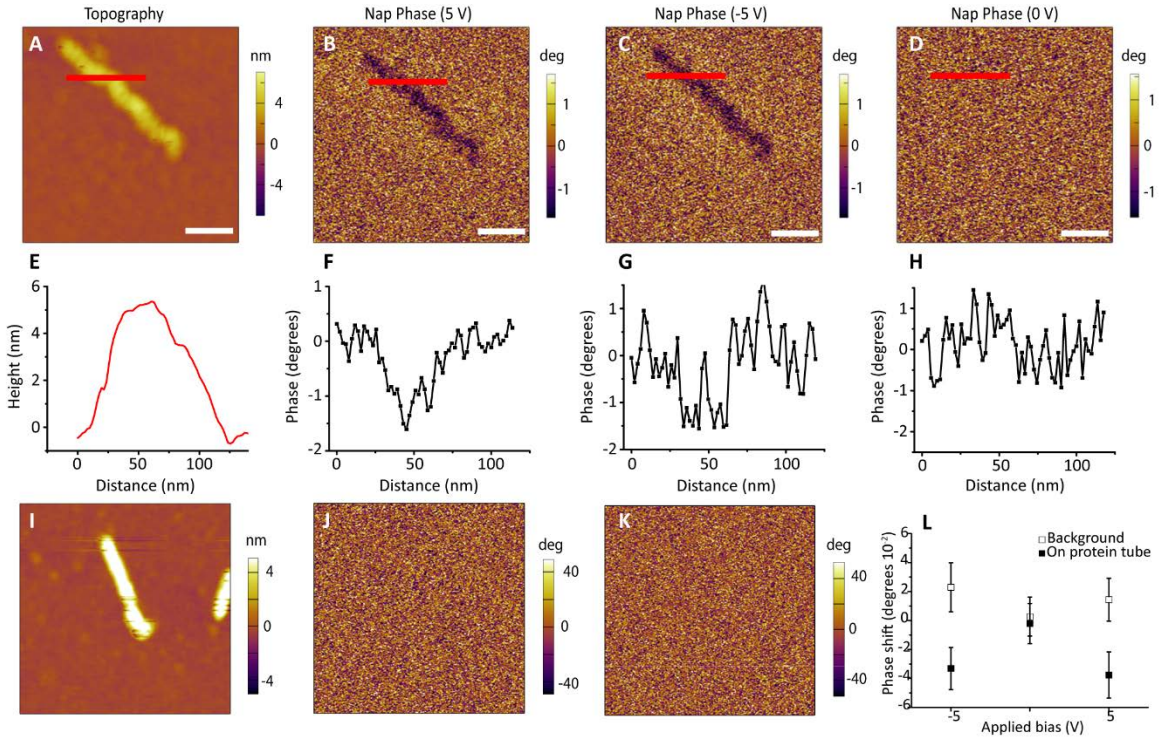

Figure 5: Data from EFM of Fe-Prx dialysed to pH 6.0 and deposited on a p-doped silicon wafer. The first pass topography is displayed in A and the second pass with a lift height of 30 nm in B-D with applied bias of 5 V, -5 V or 0 V respectively. The corresponding height and phase profiles (along the red line in the images) are presented in E-H. Topography, and Nap phase images of Prx control (I-K) .L shows the mean ± std of average phase shifts of 20 Fe-Prx tubes obtained at indicated locations at 5 different locations on the silicon wafer. Scale bars represent 60 nm.

To conclude, we have demonstrated a biomimetic approach to synthesize iron containing particles inside a protein pore, restricted in size by the protein template. Protein mineralization is facilitated by a generic histidine tag functionalized pore of the toroidal shaped peroxiredoxin protein, which catalyses iron oxidation in the presence of atmospheric oxygen. To our knowledge, this is the first time a non-cage protein was utilized to grow iron oxide cores formed by 200-300 atoms of iron. The ligand-controlled approach employed here is simple and versatile, and can likely be extended to synthesize other transition metal/metal oxide nanoparticles. The controlled stacking ability of Prx at moderately acidic pH conditions offers a straightforward way of building one-dimensional nanoparticle assemblies. Such assemblies are of interest for constructing new electronic, optical and magnetic devices. [79, 80]

Associated content:

Supporting Information

The Supporting Information is available free of charge on the ACS Publications website at DOI: 10.1021/acs.nanolett.7b04385. The supporting informaiton for this article contains full experimental materials and methods, supporting size exclusion chromatography, bulk XRD spectra and TEM, and EFM images.

Author contributions:
The manuscript was written through contributions from all authors and all authors have read and approved the final version of the manuscript.

Acknowledgements: This work is supported by the MacDiarmid Institute for Advanced Materials and Nanotechnology. Thanks to Andrew Chang for fruitful discussions on TEM imaging. Thanks to Dr. Alec Asedov for his help with XRD analysis. We thank Matt Pendred for his help in making a graphical abstract, Frankie Conroy for providing the his-tagged cleaved WtPrx and helpful discussions.

References

1. Deng, Z.; Tian, Y.; Lee, S. H.; Ribbe, A. E.; Mao, C. *Angewandte Chemie International Edition* **2005,** 44, (23), 3582-3585.
2. Routh, P.; Mukherjee, P.; Nandi, A. K. *Langmuir* **2010,** 26, (7), 5093-5100.
3. Wang, Z.-G.; Ding, B. *Accounts of chemical research* **2014,** 47, (6), 1654-1662.
4. Satyavolu, N. S. R.; Tan, L. H.; Lu, Y. *Journal of the American Chemical Society* **2016,** 138, (50), 16542-16548.
5. Edwardson, T. G. W.; Lau, K. L.; Bousmail, D.; Serpell, C. J.; Sleiman, H. F. *Nature Chemistry* **2016,** 8, 162.
6. Lawson, D. M.; Artymiuk, P. J.; Yewdall, S. J.; Smith, J. M. A.; Livingstone, J. C.; Treffry, A.; Luzzago, A.; Levi, S.; Arosio, P.; Cesareni, G.; Thomas, C. D.; Shaw, W. V.; Harrison, P. M. *Nature* **1991,** 349, (6309), 541-544.
7. Peng, T.; Paramelle, D.; Sana, B.; Lee, C. F.; Lim, S. *Small* **2014,** 10, (15), 3131-3138.
8. Clare, D. K.; Orlova, E. V. *Journal of Structural Biology* **2010,** 171, (3-3), 303-308.
9. Mougous, J. D.; Cuff, M. E.; Raunser, S.; Shen, A.; Zhou, M.; Gifford, C. A.; Goodman, A. L.; Joachimiak, G.; Ordoñez, C. L.; Lory, S.; Walz, T.; Joachimiak, A.; Mekalanos, J. J. *Science* **2006,** 312, (5779), 1526-1530.
10. Gutsche, I.; Coulibaly, F.; Voss, J. E.; Salmon, J.; d'Alayer, J.; Ermonval, M.; Larquet, E.; Charneau, P.; Krey, T.; Mégret, F.; Guittet, E.; Rey, F. A.; Flamand, M. *Proceedings of the National Academy of Sciences* **2011,** 108, (19), 8003-8008.
11. Liu, W.; Brock, A.; Chen, S.; Chen, S.; Schultz, P. G. *Nature Methods* **2007,** 4, 239.
12. Setaro, F.; Brasch, M.; Hahn, U.; Koay, M. S. T.; Cornelissen, J. J. L. M.; de la Escosura, A.; Torres, T. *Nano Letters* **2015,** 15, (2), 1245-1251.
13. Mikkilä, J.; Anaya-Plaza, E.; Liljeström, V.; Caston, J. R.; Torres, T.; de la Escosura, A.; Kostiainen, M. A. *ACS Nano* **2016,** 10, (1), 1565-1571.
14. Anh, P. T.; Andreas, S.; M., S. S.; Helmut, C. *Advanced Functional Materials* **2017,** 27, (7), 1604532.
15. Okesola, B. O.; Mata, A. *Chemical Society Reviews* **2018**.
16. Aumiller, W. M.; Uchida, M.; Douglas, T. *Chemical Society Reviews* **2018**.
17. Yeates, T. O. *Annual Review of Biophysics* **2017,** 46, (1), 23-42.
18. Allen, M.; Willits, D.; Mosolf, J.; Young, M.; Douglas, T. *Advanced Materials* **2002,** 14, (21), 1562-1565.

19. Matsumoto, Y.; Chen, R.; Anikeeva, P.; Jasanoff, A. *Nature Communications* **2015,** 6, 8721.
20. Zeth, K.; Hoiczyk, E.; Okuda, M. *Trends in Biochemical Sciences* **2016,** 41, (2), 190-203.
21. Papaefthymiou, G. C. *Magnetic Nanoparticle Assemblies* **2014**, 1.
22. Chasteen, N. D.; Harrison, P. M. *Journal of Structural Biology* **1999,** 126, (3), 182-194.
23. Jutz, G.; van Rijn, P.; Santos Miranda, B.; Böker, A. *Chemical Reviews* **2015,** 115, (4), 1653-1701.
24. Aljabali, A. A. A.; Barclay, J. E.; Lomonossoff, G. P.; Evans, D. J. *Nanoscale* **2010,** 2, (12), 2596-2600.
25. Aljabali, A. A. A.; Barclay, J. E.; Cespedes, O.; Rashid, A.; Staniland, S. S.; Lomonossoff, G. P.; Evans, D. J. *Advanced Functional Materials* **2011,** 21, (21), 4137-4142.
26. Douglas, T.; Strable, E.; Willits, D.; Aitouchen, A.; Libera, M.; Young, M. *Advanced Materials* **2002,** 14, (6), 415-418.
27. Klem, M. T.; Willits, D.; Solis, D. J.; Belcher, A. M.; Young, M.; Douglas, T. *Advanced Functional Materials* **2005,** 15, (9), 1489-1494.
28. Kramer, R. M.; Li, C.; Carter, D. C.; Stone, M. O.; Naik, R. R. *Journal of the American Chemical Society* **2004,** 126, (41), 13282-13286.
29. Hall, A.; Karplus, P. A.; Poole, L. B. *FEBS Journal* **2009,** 276, (9), 2469-2477.
30. Wood, Z. A.; Poole, L. B.; Hantgan, R. R.; Karplus, P. A. *Biochemistry* **2002,** 41, (17), 5493-5504.
31. Saccoccia, F.; Di Micco, P.; Boumis, G.; Brunori, M.; Koutris, I.; Miele, Adriana E.; Morea, V.; Sriratana, P.; Williams, David L.; Bellelli, A.; Angelucci, F. *Structure* **2012,** 20, (3), 429-439.
32. Yewdall, N. A.; Venugopal, H.; Desfosses, A.; Abrishami, V.; Yosaatmadja, Y.; Hampton, Mark B.; Gerrard, Juliet A.; Goldstone, David C.; Mitra, Alok K.; Radjainia, M. *Structure* **2016,** 24, (7), 1120-1129.
33. Domigan, L. J.; Ashmead, H.; Dimartino, S.; Malmstrom, J.; Grant Pearce, F.; Blunt, M.; Williams, D. E.; Gerrard, J. A. *Biointerphases* **2017,** 12, (4), 04E405.
34. Phillips, A. J.; Littlejohn, J.; Yewdall, N. A.; Zhu, T.; Valéry, C.; Pearce, F. G.; Mitra, A. K.; Radjainia, M.; Gerrard, J. A. *Biomacromolecules* **2014,** 15, (5), 1871-1881.
35. Radjainia, M.; Venugopal, H.; Desfosses, A.; Phillips, Amy J.; Yewdall, N. A.; Hampton, Mark B.; Gerrard, Juliet A.; Mitra, Alok K. *Structure* **2015,** 23, (5), 912-920.
36. Kostiainen, M. A.; Hiekkataipale, P.; de la Torre, J. A.; Nolte, R. J. M.; Cornelissen, J. J. L. M. *Journal of Materials Chemistry* **2011,** 21, (7), 2112-2117.
37. Kostiainen, M. A.; Kasyutich, O.; Cornelissen, J. J. L. M.; Nolte, R. J. M. *Nat Chem* **2010,** 2, (5), 394-399.
38. Kostiainen, M. A.; Ceci, P.; Fornara, M.; Hiekkataipale, P.; Kasyutich, O.; Nolte, R. J. M.; Cornelissen, J. J. L. M.; Desautels, R. D.; van Lierop, J. *ACS Nano* **2011,** 5, (8), 6394-6402.
39. Brodin, J. D.; Ambroggio, X. I.; Tang, C.; Parent, K. N.; Baker, T. S.; Tezcan, F. A. *Nature Chemistry* **2012,** 4, 375.
40. Brodin, J. D.; Carr, J. R.; Sontz, P. A.; Tezcan, F. A. *Proceedings of the National Academy of Sciences* **2014,** 111, (8), 2897-2902.
41. Biswas, S.; Kinbara, K.; Oya, N.; Ishii, N.; Taguchi, H.; Aida, T. *Journal of the American Chemical Society* **2009,** 131, (22), 7556-7557.

42. Sendai, T.; Biswas, S.; Aida, T. *Journal of the American Chemical Society* **2013,** 135, (31), 11509-11512.
43. Medalsy, I.; Dgany, O.; Sowwan, M.; Cohen, H.; Yukashevska, A.; Wolf, S. G.; Wolf, A.; Koster, A.; Almog, O.; Marton, I.; Pouny, Y.; Altman, A.; Shoseyov, O.; Porath, D. *Nano Letters* **2008,** 8, (2), 473-477.
44. Behrens, S.; Heyman, A.; Maul, R.; Essig, S.; Steigerwald, S.; Quintilla, A.; Wenzel, W.; Bürck, J.; Dgany, O.; Shoseyov, O. *Advanced Materials* **2009,** 21, (34), 3515-3519.
45. Sun, H.; Miao, L.; Li, J.; Fu, S.; An, G.; Si, C.; Dong, Z.; Luo, Q.; Yu, S.; Xu, J.; Liu, J. *ACS Nano* **2015,** 9, (5), 5461-5469.
46. Miao, L.; Fan, Q.; Zhao, L.; Qiao, Q.; Zhang, X.; Hou, C.; Xu, J.; Luo, Q.; Liu, J. *Chemical Communications* **2016,** 52, (21), 4092-4095.
47. McMillan, R. A.; Howard, J.; Zaluzec, N. J.; Kagawa, H. K.; Mogul, R.; Li, Y.-F.; Paavola, C. D.; Trent, J. D. *Journal of the American Chemical Society* **2005,** 127, (9), 2800-2801.
48. Schreiber, A.; Huber, M. C.; Cölfen, H.; Schiller, S. M. **2015,** 6, 6705.
49. Young, M.; Debbie, W.; Uchida, M.; Douglas, T. *Annual Review of Phytopathology* **2008,** 46, (1), 361-384.
50. Knez, M.; Kadri, A.; Wege, C.; Gösele, U.; Jeske, H.; Nielsch, K. *Nano Letters* **2006,** 6, (6), 1172-1177.
51. Liu, Y.; Xu, Y.; Zhu, Y.; Culver, J. N.; Lundgren, C. A.; Xu, K.; Wang, C. *ACS Nano* **2013,** 7, (4), 3627-3634.
52. Knez, M.; Bittner, A. M.; Boes, F.; Wege, C.; Jeske, H.; Maiβ, E.; Kern, K. *Nano Letters* **2003,** 3, (8), 1079-1082.
53. Tsukamoto, R.; Muraoka, M.; Seki, M.; Tabata, H.; Yamashita, I. *Chemistry of Materials* **2007,** 19, (10), 2389-2391.
54. Wayne, S.; Trevor, D.; Mark, Y.; Gerald, S.; Stephen, M. *Advanced Materials* **1999,** 11, (3), 253-256.
55. Dujardin, E.; Peet, C.; Stubbs, G.; Culver, J. N.; Mann, S. *Nano Letters* **2003,** 3, (3), 413-417.
56. Ardini, M.; Giansanti, F.; Di Leandro, L.; Pitari, G.; Cimini, A.; Ottaviano, L.; Donarelli, M.; Santucci, S.; Angelucci, F.; Ippoliti, R. *Nanoscale* **2014,** 6, (14), 8052-8061.
57. Ardini, M.; Golia, G.; Passaretti, P.; Cimini, A.; Pitari, G.; Giansanti, F.; Leandro, L. D.; Ottaviano, L.; Perrozzi, F.; Santucci, S.; Morandi, V.; Ortolani, L.; Christian, M.; Treossi, E.; Palermo, V.; Angelucci, F.; Ippoliti, R. *Nanoscale* **2016,** 8, (12), 6739-6753.
58. Oaki, Y.; Yagita, N.; Imai, H. *Chemistry – A European Journal* **2012,** 18, (1), 110-116.
59. Yagita, N.; Oaki, Y.; Imai, H. *Chemistry – A European Journal* **2013,** 19, (14), 4419-4422.
60. Sundberg, R. J.; Martin, R. B. *Chemical Reviews* **1974,** 74, (4), 471-517.
61. Raymond, K. N.; Allred, B. E.; Sia, A. K. *Accounts of Chemical Research* **2015,** 48, (9), 2496-2505.
62. Pham, A. N.; Waite, T. D. *The Journal of Physical Chemistry A* **2008,** 112, (4), 643-651.
63. Krishnamurti, G. S. R.; Huang, P. M. *Clays and Clay Minerals* **1991,** 39, (1), 28-34.
64. Furia, T. E., *CRC Handbook of Food Additives, Second Edition*. Taylor & Francis: 1973.

65. Ceci, P.; Chiancone, E.; Kasyutich, O.; Bellapadrona, G.; Castelli, L.; Fittipaldi, M.; Gatteschi, D.; Innocenti, C.; Sangregorio, C. *Chemistry – A European Journal* **2009,** 16, (2), 709-717.
66. Xu, S.; Arnsdorf, M. F. *Journal of Microscopy* **1994,** 173, (3), 199-210.
67. Jaafar, M.; Aljabali, A. A. A.; Berlanga, I.; Mas-Ballesté, R.; Saxena, P.; Warren, S.; Lomonossoff, G. P.; Evans, D. J.; de Pablo, P. J. *ACS Applied Materials & Interfaces* **2014,** 6, (23), 20936-20942.
68. Malmstrom, J.; Wason, A.; Roache, F.; Yewdall, N. A.; Radjainia, M.; Wei, S.; Higgins, M. J.; Williams, D. E.; Gerrard, J. A.; Travas-Sejdic, J. *Nanoscale* **2015,** 7, (47), 19940-19948.
69. Cox, M. M.; Nelson, D. L., *Lehninger principles of biochemistry*. WH Freeman: 2008.
70. Janney, D. E.; Cowley, J. M.; Buseck, P. R. *Clays and Clay Minerals* **2000,** 48, (1), 111-119.
71. Banfield, J. F.; Welch, S. A.; Zhang, H.; Ebert, T. T.; Penn, R. L. *Science* **2000,** 289, (5480), 751-754.
72. Flenniken, M. L.; Willits, D. A.; Brumfield, S.; Young, M. J.; Douglas, T. *Nano Letters* **2003,** 3, (11), 1573-1576.
73. Bhushan, B., *Scanning probe microscopy in nanoscience and nanotechnology 2*. Springer Science & Business Media: 2010.
74. Cohen, H.; Sapir, T.; Borovok, N.; Molotsky, T.; Di Felice, R.; Kotlyar, A. B.; Porath, D. *Nano Letters* **2007,** 7, (4), 981-986.
75. Malvankar, N. S.; Yalcin, S. E.; Tuominen, M. T.; Lovley, D. R. *Nature Nanotechnology* **2014,** 9, 1012.
76. Ceci, P.; Chiancone, E.; Kasyutich, O.; Bellapadrona, G.; Castelli, L.; Fittipaldi, M.; Gatteschi, D.; Innocenti, C.; Sangregorio, C. *Chemistry – A European Journal* **2010,** 16, (2), 709-717.
77. Jiang, T.; Vail, O. A.; Jiang, Z.; Zuo, X.; Conticello, V. P. *Journal of the American Chemical Society* **2015,** 137, (24), 7793-7802.
78. Iwaura, R. *Soft Matter* **2017,** 13, (44), 8293-8299.
79. Tang, Z.; Kotov, N. A. *Advanced Materials* **2005,** 17, (8), 951-962.
80. Shipway, A. N.; Katz, E.; Willner, I. *ChemPhysChem* **2000,** 1, (1), 18-52.